International Journal of Thermodynamics (IJoT)
ISSN 1301-9724 / e-ISSN 2146-1511
https://dergipark.org.tr/en/pub/ijot

Vol. 26 (No. 2), pp. 001-011, 2023
doi: 10.5541/ijot.1097756
Published online: June 1, 2023

Research Article

Semi-Analytical Solution for Modelling Moving Heat Sources in a Semi-Infinite Medium with Radiative and Convective Boundary Conditions

*A. Metallo

Industrial Engineering Department, University of Salerno, Italy
E-mail: antonio.metallo@libero.it

Received 3 April 2022, Revised 22 February 2023, Accepted 22 February 2023

Abstract

The weld quality is highly related to the thermal history of the weld and there have been many trials to monitor the quality using an infrared (IR) sensor. To obtain the real temperature of a surface based on the brightness temperature values measured by an IR camera, the emissivity value must be derived. For an accurate assessment of the emissivity, one must be aware of the melting point isotherm. The temperature profiles only depend on three factors during laser processing, specified as constants the characteristics of the material: laser beam speed (v), laser beam diameter (d), and power (P). Predicting the width of the melted zone reached during the welding process as the parameters vary is a tool for helping a quality laser processing and for determination of true temperature in laser welding using IR camera. This study describes the semi-analytical (SA) solution of the heat conduction equation for a localized moving Gaussian heat source with constant parameters on a semi-infinite medium. The solution, simple and quick to obtain, provides information on the width of the melted zone with an average error < 5 %. The outcome is assessed numerically and contrasted with FEM solutions for a Gaussian source, the latter having undergone experimental validation. With two distinct defocus values, def_0 and def_{-6}, and by varying the speed and power settings, two separate types of experiments were run. Thus, the SA solution was obtained and compared after the FEM solution had been obtained with a good approximation (max err 4.3 %, average err 2.7 %). Only in regard to the 1AL test is an error more than 5 % detected; in the other case, the average error is 3.75 %. Two more tests at the defocus values of def-4 and def-8 were conducted to confirm the model's validity as the parameters varied. Overall, the average error between the semi-analytical and the FEM solution is 4.1%. The SA solution may be used to effectively estimate the isotherms related to the melting point of aluminum (770 K). This allows to obtain a tool which helps restoring the real temperature based on the brightness values measured by the IR camera during laser welding. At the same time, this effective tool allows to investigate the importance of different processing parameters in laser manufacturing.

Keywords: *Semi-analytical solution; laser welding; integral method; semi-infinite medium.*

1. Introduction

The temperature of the object, including laser welding is one of the key parameters of thermal processes [1,2]. The temperature and temperature gradient determine the speed of phase transitions, chemical reactions, microstructure and properties of the material [3]. During laser processing, defined as constants the properties of the material, the temperature profiles depend exclusively on three parameters: laser beam speed (v) , laser beam diameter (d) and power (P).

Predicting temperatures reached during the welding process as the parameters vary is a tool for helping a quality laser processing and for determination of true temperature in laser welding using IR camera [4-5]. To restore the real temperature, based on the brightness temperature values measured by the IR camera, the emissivity must be evaluated. For this purpose, firstly, the isotherms corresponding to the melting point were calculated to compare it with the temperature distribution measured in the laser irradiation zone. The calculated and measured data were compared with the width of the melted zone. Using the melting point isotherm, the value of emissivity could be calculated, and the true temperature could be restored [6,24].

The phenomenon of laser welding has been the subject of extensive experimental and analytical study. Rosenthal [25] and Rykalin et al. [26] have studied classical solutions of the heat conduction equations. A complete reference book with analytical solutions to the heat conduction equation has been created by Carslaw and Jaeger [27]. The heat sources used in this study are point sources, line sources and plane sources since these types of geometry offer the most straightforward analytical solutions. These sources are well adapted to forecast the thermal history far from the source. They are useless, however, if they are close to the heat source as the temperature would would become infinite. Eagar and Tsai [28] introduced 2D heat sources to address this issue. The first to introduce a 3D heat source, was Goldak et al. [29]. He employed finite element modeling to determine the temperature field using a pair of moving ellipsoids as heat sources. A closed form analytical solution for these types of 3D heat sources in a thick plate or a semi-infinite body was recently developed by Nguyen et al. [30,31]. The solution is particularly difficult since the mirror image approach must be employed when applying it on the finished slabs. The detailed derivation of the analytical approximation solution

*Corresponding Author

for a double ellipsoidal density heat source in a finite thick plate is described by M. Van Elsen et al. in detail [32]. In this instance, the solution for the transient temperature field was determined using a complicated and time-consuming numerical approach. Thomas F. Flint et al. [33] and R.T. Forslunda et al. [34] both proposed analytical solutions that take into account a moving Gaussian heat flow and a double ellipsoidal volumetric heat source, respectively. The solutions in this case, in addition to being time-consuming, only explain the transient temperature field in the components without evaluated the width of the melted zone.

The proposed SA solution simplifies the calculation of the width of the melted zone and eliminates the need for laborious numerical procedures. Using the SA solution it is possible to evaluate the isotherms corresponding to the melting point as the parameters vary. The solutions obtained approximating with a very small error (err < 5 %) the width of the melted zone. The use of a FEM model, modeled and validated by comparison with the laser tests, is certainly an alternative, but in any case presents much longer calculation times if referred to the semi-analytical solution. The solution is presented based on some assumptions and linearization.

.

2. Mathematical Model

A mathematical model of heat conduction overlap welding by a laser beam was developed. Assumptions and simplifications were made to reduce computational cost. As we are purely interested in the evaluation of the melting point isotherm and not other aspects, for example such as, the depth of penetration (key hole) or the study of phenomena concerning the phase change or evaporation, this assumptions can be considered valid. The main simplifications of the model are presented and discussed below;

• The phase transformations and in turn the latent heats of melting and solidification are ignored. This causes somewhat overestimated temperatures around the melting isotherm (which should consume latent heat) and vice versa underestimated temperatures around the solidification isotherm. Usually, the temperature in the central melt pool domain becomes somewhat too high. This simplification is justified by the reason that we are interested in the evaluation of the width of the melted zone.

• Thermophysical material properties are assumed to be temperature independent (though suitable mean values can be chosen in place of the values for ambient temperature).

• The heat source moves with constant speed v along x axis and its center coincide with the origin of the moving Cartesian x-y coordinate system at surface z=0 (Figure 1).

The beam power density profile $\dot{q}(x,y)$ is modelled by spatially superimposing several Gaussian beams in a suitable manner: $\dot{q}_g(x,y)=\frac{2\cdot P}{\pi\cdot r_0^2}\mathrm{Exp}\left(-\frac{2\cdot r^2}{r_0^2}\right)$ wit $r=\sqrt{x^2+y^2}$.

The work piece has six faces where boundary conditions have to be specified. At the bottom surface z = ε and on the four lateral faces the condition of thermal insulation has been assumed, and at the top surface z = 0, a combined Gaussian source ($\dot{q}_g$) and convection-radiation boundary condition is assumed (Figure 1). The medium is assumed initially in equilibrium with the ambient at temperature $T_0 = T_\infty$.

Given the above information, the problem can now be formulated as follows. The three-dimensional, transient heat conduction equation is:

$$\frac{\partial^2 T}{\partial x^2}+\frac{\partial^2 T}{\partial y^2}+\frac{\partial^2 T}{\partial z^2}=\frac{1}{\alpha}\frac{\partial T}{\partial t} \tag{1}$$

where α is the thermal diffusivity which is described by α = k/(ρ cp) , k is the thermal conductivity, ρ is the mass density and cp the specific heat. The initial and boundary conditions are written as:

$$T\ x,y,z,0\ =T_\infty \tag{2}$$

$$\left.\frac{\partial T}{\partial x}\right|_{x=-\frac{L}{2}}=0 \tag{3}$$

$$\left.\frac{\partial T}{\partial x}\right|_{x=\frac{L}{2}}=0 \tag{4}$$

$$\left.\frac{\partial T}{\partial y}\right|_{y=-\frac{L}{2}}=0 \tag{5}$$

$$\left.\frac{\partial T}{\partial y}\right|_{y=\frac{L}{2}}=0 \tag{6}$$

$$k\left.\frac{\partial T}{\partial z}\right|_{z=0}=-\dot{q}_{gauss}+h\cdot\ T(x,y,0,t)-T_\infty +\varepsilon\cdot\sigma\cdot\ T^4(x,y,0,t)-T_\infty^4 \tag{7}$$

$$\left.\frac{\partial T}{\partial z}\right|_{z=\varepsilon}=0 \tag{8}$$

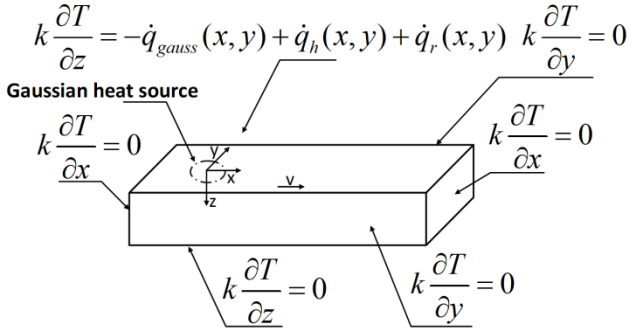

Figure 1. Model for analysis of the moving source of a bar.

If a coordinate system fixed to the heat source is chosen, according to the moving heat source theory [7], a mathematical statement of the three dimensional thermal conductive problem is:

$$\frac{\partial^2 T}{\partial x^2}+\frac{\partial^2 T}{\partial y^2}+\frac{\partial^2 T}{\partial z^2}=\frac{1}{\alpha}\left(\frac{\partial T}{\partial t}-v\frac{\partial T}{\partial x}\right) \tag{9}$$

The dimensionless energy balance equation and the related boundary conditions lead to a non-homogeneous linear problem:

$$\frac{\partial^2\theta}{\partial\xi^2}+\frac{\partial^2\theta}{\partial\psi^2}+\frac{\partial^2\theta}{\partial\zeta^2}=\frac{\partial\theta}{\partial\tau}-\frac{\partial\theta}{\partial\xi} \quad (10)$$

$$\left.\frac{\partial\theta}{\partial\xi}\right|_{\xi=-\infty}=0 \quad (11)$$

$$\left.\frac{\partial\theta}{\partial\xi}\right|_{\xi=\infty}=0 \quad (12)$$

$$\left.\frac{\partial\theta}{\partial\psi}\right|_{\psi=-\infty}=0 \quad (13)$$

$$\left.\frac{\partial\theta}{\partial\psi}\right|_{\psi=\infty}=0 \quad (14)$$

$$\left.\frac{\partial\theta}{\partial\zeta}\right|_{\zeta=0}=-\frac{1}{\upsilon}Exp\left(-2\frac{\sigma^2}{\sigma_0^2}\right)+Bi\cdot\theta(\xi,\psi,0)+A_1\cdot\theta^4(\xi,\psi,0) \quad (15)$$

$$\left.\frac{\partial\theta}{\partial\zeta}\right|_{\zeta=\infty}=0 \quad (16)$$

$$\theta\ \xi,\psi,\zeta,0\ =0 \quad (17)$$

where the following dimensionless parameters have been introduced: $\theta=(T-T_\infty)/\Delta T_{ref}$ is the temperature; the group $\Delta T_{ref} = C_{abs}\cdot P/(\pi\cdot k\cdot r_0)$ is a reference temperature difference withC_{abs} representing the absorption coefficient, a reference length $x_{ref} =\alpha/v$ and a reference radius $r_{ref} = P_1\cdot x_{ref}$ where P_1 represents the proportionality coefficient. In this way it was possible to obtain a solution that best approximates both the maximum temperature profile and the fusion isotherm; the reference time is $t_{ref}=x_{ref}^2/\alpha$ and reference velocity $v_{ref}=2\cdot\alpha/r_0$. The dimensionless space variable was defined such as $\xi=\frac{x}{x_{ref}}$; $\psi=\frac{y}{x_{ref}}$; $\zeta=\frac{z}{x_{ref}}$; $\sigma=r/r_{ref}$, and the dimensionless time resulted $\tau=r_{ref}/t_{ref}$. Finally, dimensionless velocity resulted $v = v/v_{ref}$, $Bi=h\cdot x_{ref}/k$ is the Biot number and $A_1=\varepsilon\cdot\sigma\cdot x_{ref}\cdot\Delta T_{ref}^3/k$ is a dimensionless coefficient. The semi-infinite slab model is justified because x_{ref} is small compared to the sample size. Thus, it is possible to simplify the problem and evaluate a stationary solution.

3. Materials and Method

It was considered a base metal corresponding to the standard EN 45100 aluminum (Table 1). For the purposes of this work, a Yb: YAG disk laser source supplied in fiber, operating in continuous wave emission, was considered (Table 2). The movement of the laser head was performed by a 6-axis industrial robot with a dedicated controller, and an integrated 3-way power nozzle was attached to the laser head (Figure 2).

Argon was injected as a carrier gas at a flow rate of 30 L / min. The helium was coaxially blown to the laser beam at a flow rate of 10 L / min as a shielding gas on the melting bath.

A tilt angle of 4◦ was set for the laser head, in accordance with common practice for processing highly reflective metals [8] to prevent rear reflections from entering the optical train. We have therefore been defined the main governance parameters and the crucial response variables to consider [9,23].

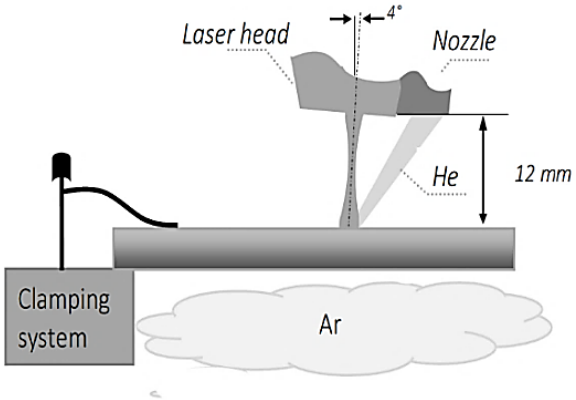

Figure 2. Schematic of the laser head with three-way feed nozzle; components not to scale.

Table 1. Nominal Chemical Composition (wt %) of Base Metals.

chemical components	%
Si	4.5÷6
Fe	0.5
Cu	2.6÷*3.6*
Mn	0.55
Mg	0.20÷*0.45*
Cr	/
Ni	0.1
Zn	0.1
Sn	0.05
Ti	0.2

This choice is usually based on both the literature and past experience. Many variables are involved in laser welding, primarily, power and welding speed since they determine the heat input to the work-piece [10].

Table 2. Welding System Technical Data.

Maximum output power [kW]	4.0
Laser light wavelength λ [nm]	1030
Beam Parameter Product [nm x mrad]	8.0
Focal beam waist d [mm]	0.3
Rayleigh range [mm]	2.81
Focal length f [mm]	200
Maximum power density [kW/mm2]	56.6
Laser beam diameter at defocus 0 [mm]	0.3
Laser beam diameter at defocus -2 [mm]	0.44
Laser beam diameter at defocus -4 [mm]	0.71
Laser beam diameter at defocus -6 [mm]	1.11
Laser beam diameter at defocus -8 [mm]	1.32

In addition, successful laser welding requires the optimization of other parameters such as the size and the location of the focal spot. Thus, finally, defocusing d (the distance of the focal point with respect to the top surface) has been included in the experimental plan.

The range for power in the experimental plan has been decided so that the specific threshold irradiance for conduction to key-hole transition would be overcome. Sensible values for welding speed have been found via

preliminary trials in the form of bead-on-plate tests aiming at producing full penetration with no significant drop-through on the lower surface, thus matching the requirements as defined in the referred standard [11].

3.1. Numerical Modeling: Finite Element Method.

The FEM model was built using COMSOL Multiphysics software. For the correct construction of the model have been defined:

Model parameters: needed to build the numerical model such as the type of materials, sample size, wavelength , and work parameters: power, scan speed and laser beam diameter (Table. 2).

Materials' Properties: as we are interested at the temperature profile corresponding to the melting isotherm, which then develops inside the melting zone, we have chosen to use the properties at the melting temperature value for both the specific heat and the thermal conductivity coefficient [12-13], both as regards density [14-15] (Table. 1b). The absorption values were chosen for aluminum 0.23 [16,17] .

Geometry and mesh modeling: One of the most important steps in FEM modeling is the definition of the mesh geometry. The geometry of the model consists of two thin sheets. A 3-D solid blocks of (40 x 30 x 6) mm^3 were created. Several different grid distributions have been tested to ensure that the calculated results are grid independent. Maximum temperature differences of the fields are less than 0.1 precent by doubling the mesh nodes. The two parts are meshed using tetrahedral geometry meshes. The minimum and maximum size of the element for the mesh is 0.1 and 0.15 mm for the block where one boundary condition has been applied and 0.15 and 0.5 mm for the other (Figure 3). The complete mesh consists of 2659767 volume elements, 258806 surface elements, and 1184 elements for upper block and of 4242245 volume elements, 281738surface elements, and 2212 elements lower block.

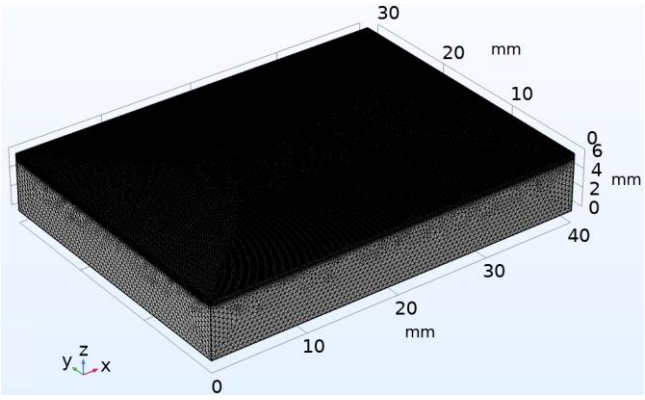

Figure 3. The minimum and maximum size of the element for the mesh.

Boundary conditions and initial condition: The laser beam incident on the surface z = 0 was characterized by a second type boundary condition where the imposed flux is the heat source. In addition, the third type boundary condition on face z = 0 was considered. In the hypothesis of natural convection, the model was given a constant thermal convection coefficient h = 10 W m^{-2} K^{-1} [18-21]. It was also considering radiative cooling: a constant value was set ε = 0.1 [17] for aluminum. Furthermore, the condition of thermal insulation has been assumed on the remaining surfaces. The ambient temperature and the initial temperature conditions of the plate are equal to 293 K. Ultimately, the generation of plasma, and hence the attenuation of the beam, can be neglected since in this application, vaporization is prevented [22].

Laser beam modeling: Let us consider a thin layer, infinite in the x and y dimensions, with a thickness in the z dimension. We establish the coordinate system in such a way that the top surface of the layer is at z = 0 and the bottom surface is at z = L_z (Figure 4).

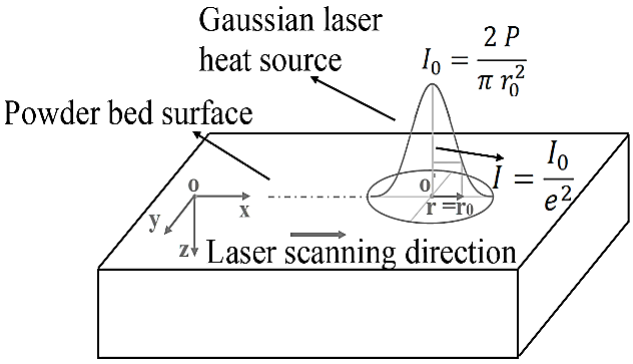

Figure 4. Sketch of the workpiece and coordinate system.

We assume that in the z-direction the heat source is concentrated at a level immediately below the upper surface (z = 0). The irradiation of the beam gradually decreases at the edges.

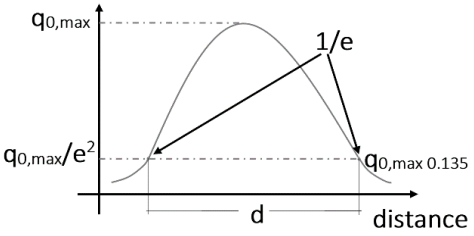

Figure 5. Gauss laser beam modelling.

Table 3. Gauss Laser Beam Modeling.

	Power in Range[%]
$\frac{2 \cdot P}{\pi \cdot r_0^{\,2}} Exp\left(-\frac{2 \cdot \left((x-x_0)^2+(y-y_0)^2\right)}{r_0^{\,2}}\right)$	89

To define beam width for Gaussian beams was used a 1/e2 method. The width of the beam is calculated by measuring the distance between the two points where the intensity is 1/e2 of the peak value (Figure 5, Table 3). So only about 86.5 % of the laser power is contained within the 1/e2 width (Eq. (18)).

$$\int_{x=-\sigma}^{\sigma} \int_{y=-\sigma}^{\sigma} \dot{q}_{gauss}(x,y) \cdot dxdy = 86.5\ \%\ P \qquad (18)$$

4. Result and Discussion

4.1 Experimental Tests

Two types of tests were carried out at different defocus values as shown in Table 4. A rectangular section plate of sizes (Lx=100 x Ly=50 x Lz=6 mm) was used.

Each test was analyzed under an electron microscope which made it possible to obtain an image of the trace in TIF format (Figure 6). The traces were divided 17 parts at 4 mm

intervals. For each section the size of the trace , mean values and standard deviations were evaluated (Table 5).

Table 4. Welding system technical data.

	Power P [W]	welding speed v [mm s-1]	Defocus def [mm]	Beam Diameter d [mm]
1AL	2500	50	0	0.30
2AL	3000	50	0	0.30
3AL	3000	35	0	0.30
5AL	3500	50	-6	1.01
8AL	3750	40	-6	1.01
9AL	4000	40	-6	1.1

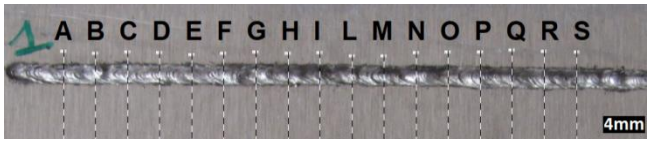

Figure 6. Test 1AL Width of the Melted Zone Sections.

Table 5. Mean Value of a Width of the Melted Zone 1AL.

Sez.	s[mm]	Sez.	s[mm]
a	2.26	m	2.57
b	2.34	n	2.49
c	2.34	o	2.44
d	2.16	p	2.57
e	2.34	q	2.39
f	2.55	r	2.39
g	2.34	s	2.39
h	2.49	Mean	2.40
i	2.34	Dev.St	0.11
l	2.31		

These results (Table 6) will be used to validate the numerical model. For this purpose the isotherms corresponding to the melting point (ρ_y) were calculated used through the finite element method.

Table 6. Mean Value of a Width of the Melted Zone

Test	Width of the melted zone w_z [mm]	Dev. st
1AL	2.40	0.11
2AL	2.58	0.15
3AL	2.88	0.15
5AL	2.87	0.10
8AL	3.18	0.13
9AL	3.40	0.08

The calculated ρ_y data were compared with the width of the melted zone (w_z).

4.2 FEM Result

The simulation process allowed us to extrapolate the maximum temperature and the values corresponding to the fusion isotherm (770 K) on the plane at z = 0 (Figure 7).

The data were fitted using an ellipsoidal model (Tables 7-8) where the coefficients have been defined in (Table 9).

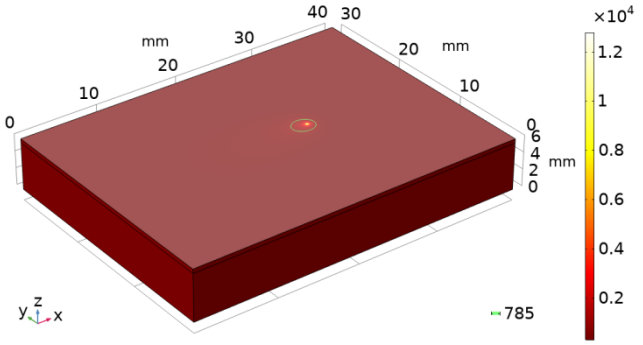

Figure 7. FE.M result: Test 1AL weld track.

Table 7. Coordinate of the Best Fit Ellipse.

$$x(r) = X_0 + a \cdot \cos\theta_r$$
$$y(r) = Y_0 + b \cdot \sin\theta_r$$
$$0 \le \theta_r \le 2 \cdot \pi$$

Table 8. Structure that Defines the Best Fit Ellipse.

a	sub axis (radius) of the X axis of the non-tilt ellipse
b	sub axis (radius) of the Y axis of the non-tilt ellipse
φ	orientation in radians of the ellipse (tilt)
X_0	center at the X axis of the non-tilt ellipse
Y_0	center at the Y axis of the non-tilt ellipse
ρ_x	size of the long axis of the ellipse
ρ_y	size of the short axis of the ellipse

In this way it was possible to quickly obtain the value of the diameter of the isotherms corresponding to the melting ρ_y.

Table 9. Fit Parameter FEM.

	1AL.	2AL	3AL	5AL	8AL	9AL
a	1.372	1.573	1.519	1.733	1.803	1.881
b	1.159	1.324	1.378	1.481	1.600	1.664
X_0	9.525	9.401	8.057	9.326	8.380	8.339
Y_0	9.999	9.999	10.000	9.999	10.000	9.999
ρ_x	2.744	3.147	3.038	3.467	3.607	3.763
ρ_y	2.318	2.649	2.756	2.961	3.201	3.329
Err %	0.110	0.257	0.419	0.075	0.093	0.184
Tmax [K]	5977	6418	6823	14294	1694	17096
Dev.St [K]	45	57	50	320	290	300

As shown in the figure for the type of test with defocus 0, being characterized by a smaller spot diameter, they have a higher power concentration, which translates into higher temperature profiles as regards the maximum temperature (Figures 8-9, Table 9).

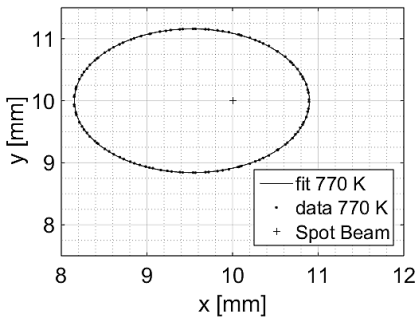

Figure 8. Test 1AL, isotherms corresponding to the melting point, FEM data fit at time = 0.1 s.

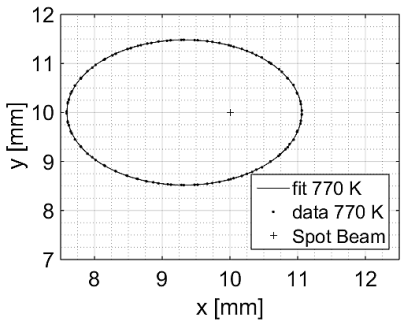

Figure 9. Test 5AL, isotherms corresponding to the melting point, FEM data fit at time = 0.1 s; T_{max} on z=0 plane.

In addition, to the same spot beam, the extension of the melted zone and therefore the diameter of the fusion isotherm increases as the maximum temperature reached increases. As shown in Figure 10,

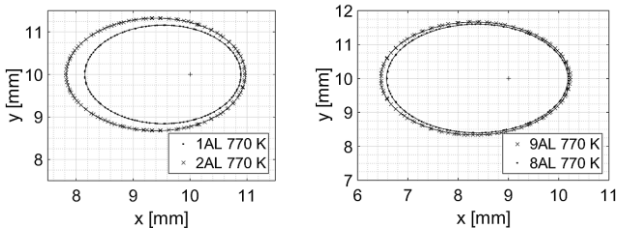

Figure 10. Comparison between isotherms corresponding to the melting point FEM test 1AL vs 2AL;8AL vs 9AL.

fixed beam diameter and scan speed, as the power delivered by the laser increases, the T_{max} and the extension of the diameter corresponding to the melting temperature increase. Once the beam diameter and laser power are fixed, the maximum temperature reached during laser welding increases as the scan speed decreases. Consequently, the diameter ρ_y also increases with decreasing speed (Figure 11).

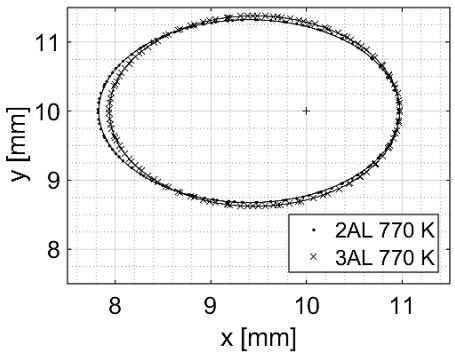

Figure 11. Comparison between isotherms corresponding to the melting point, FEM test 2AL vs 3AL.

The timing of the transient extinction is very little, about 0.01 s for defocus def_0 and 0.04 s for defocus def_{-6}, just as we expected. Therefore, for each test, the percentage error between the isotherms corresponding to the melting point (ρ_y numerically evaluated) and the extension of the melted zone (w_z, obtained through experimental tests) was evaluated.

As shown in the Table 10, the error for all types of tests presents an error below 5%. Thus, we can say that the constructed FEM model can provide a useful approximation to reality with a low average error.

Table 10. Isotherm Corresponding to the Melting Point Compared with the Width of the Melted Zone.

	Tmax[K]	Dev.st	ρy	wz	Err %
1AL	14294	320	2.3183	2.40	3.46
2AL	16945	290	2.6490	2.58	2.64
3AL	17096	300	2.7568	2.88	4.37
5AL	5977.8	45	2.9619	2.87	3.15
8AL	6418.9	57	3.2010	3.18	0.65
9AL	6823.8	50	3.3293	3.40	2.10

4.3 Semi-Analytical Solution

In order to linearize the radiative boundary condition, an average temperature was chosen to ensure that the relationship between the radiative and the convective contribution remains approximately the same.

$$\dot{Q}_r = 4\cdot\varepsilon\cdot\sigma\cdot A\ T^4(x,y,z,t) - T_p^4 \approx 10^{-1}\cdot 10^{-8}\cdot 10^{-5}\cdot 10^{16} = 10^2 \tag{19}$$

$$\dot{Q}_c \approx 10\cdot 10^{-5}\cdot 10^4 = 1 \tag{20}$$

As it is possible to observe the ratio between $\frac{\dot{Q}_r}{\dot{Q}_c} = 100$. Consequently

$$\frac{\dot{Q}_r}{\dot{Q}_c} = \frac{h_r A\ T^4(x,y,z,t) - T_p^4}{h_c A\ T^4(x,y,z,t) - T_p^4} = \frac{h_r}{h_c} = 100 \tag{21}$$

The temperature that would allow to obtain a radiative heat exchange coefficient about 100 times the convective one was therefore chosen as the reference temperature for the linearization. Since a convective heat exchange coefficient of $10\,\frac{W}{m^2\cdot K}$ was chosen:

$$\dot{Q}_{r,l} = h_r A\ T^4(x,y,z,t) - T_p^4 \tag{22}$$

$$T_r = 4000\ K \Rightarrow h_r = 4\cdot\varepsilon\cdot\sigma\cdot T_r^3 \approx 10^3\left[\frac{W}{m^2 K}\right] \tag{23}$$

In this way the ratio between radiatively and convectively exchanged thermal power is kept unchanged, with the advantage of being able to linearize the radiative boundary condition as follows:

$$\left.\frac{\partial\theta}{\partial\zeta}\right|_{\zeta=0} = -\frac{1}{\upsilon} Exp\left(-2\frac{\sigma^2}{\sigma_0^2}\right) + Bi\cdot\theta(\xi,\psi,0) + Bi_r\cdot\theta(\xi,\psi,0) \tag{24}$$

Since the problem is linear, in stationary case, the solution can be sought as the sum of two partial solutions $\theta_1(\zeta)$ and $\theta_2(\xi,\psi)$, with the first affected by a non-homogeneity arising from the Gaussian heating source. Then, the two partial solutions have to satisfy two distinct problems derived from the basic one:

$$\begin{cases} \dfrac{\partial^2\theta_1}{\partial\zeta^2}=0 \\ \left.\dfrac{\partial\theta_1}{\partial\zeta}\right|_{\zeta=0} = -\dfrac{1}{\upsilon}Exp\left(-2\dfrac{\sigma^2}{\sigma_0^2}\right) \\ \qquad\qquad +Bi\cdot\theta_1\ 0\ +Bi_r\cdot\theta_1(0) \\ \left.\dfrac{\partial\theta_1}{\partial\zeta}\right|_{\zeta=3}=0 \end{cases} \tag{25}$$

$$\begin{cases} \dfrac{\partial^2\theta_2}{\partial\xi^2}+\dfrac{\partial^2\theta_2}{\partial\psi^2}+\dfrac{\partial\theta_2}{\partial\xi}=0 \\ \left.\dfrac{\partial\theta_2}{\partial\xi}\right|_{\xi=-3}=0 \\ \left.\dfrac{\partial\theta_2}{\partial\xi}\right|_{\xi=3}=0 \\ \left.\dfrac{\partial\theta_2}{\partial\psi}\right|_{\psi=-3}=0 \\ \left.\dfrac{\partial\theta_2}{\partial\psi}\right|_{\psi=3}=0 \end{cases} \tag{26}$$

Numerically, the value 3 has been chosen as the extreme of integration to infinity, as it has been verified that at the value of 3 x_{ref} the temperature remains almost fixed at the initial value. The analytical solution of the problem 1.1a was obtained:

$$\theta_1\ \zeta\ = -\frac{e^{-2\frac{\sigma_r^2}{\sigma_0^2}}\ -3+\zeta}{\upsilon\cdot\ 1+3Bi+3Bi_r} \tag{27}$$

The second problem was solved by applying the integral method. It was possible to obtain the solution of problem 2 by choosing an approximate solution that makes explicit the dependence of the spatial variable:

$$\theta_2^+\ \xi,\psi\ = a\ \psi\ \cdot Exp\left(-\upsilon\frac{\xi+\psi}{P_2}\right) \tag{28}$$

Equation 2 has been integrated into the spatial coordinate and ξ:

$$\int_{\xi=0}^{\xi=3}\left(\frac{\partial^2\theta_2}{\partial\xi^2}+\frac{\partial^2\theta_2}{\partial\psi^2}+\frac{\partial\theta_2}{\partial\xi}\right)\cdot d\xi=0 \tag{29}$$

By imposing that the approximate analytic equation satisfies the integral and applying a boundary conditions, we obtain:

$$\frac{\left(\exp\left(-\frac{\upsilon\cdot\psi}{P_2}\right)-\exp\left(\frac{\upsilon\cdot\ 3-\psi}{P_2}\right)\right)}{P_2\cdot\upsilon}\cdot\ \upsilon\cdot\ -P_2+2\cdot\upsilon\ \cdot \\ a\ \psi\ +P_2\cdot\ -2\cdot\upsilon\cdot a'\ \psi\ +P_2\cdot a''\ \psi \tag{30}$$

$$b.c.1\quad \left.\frac{\partial\ \theta_1\ \zeta\ +\theta_2^+\ \xi,\psi}{\partial\psi}\right|_{\psi=0}=0 \\ \Rightarrow -\frac{\exp\left(-\frac{\upsilon\cdot\xi}{P_2}\right)\cdot\upsilon\cdot a\ 0}{P_2}+\exp\left(-\frac{\upsilon\cdot\xi}{P_2}\right)\cdot a'\ 0\ =0 \tag{31}$$

$$b.c.2\quad \theta_1\ \zeta\ +\theta_2^+\ \xi,3\ =0 \\ \Rightarrow -\frac{\exp\left(-\frac{2\cdot\sigma_r^2}{\sigma_0^2}\right)\cdot\ -3+\zeta}{\upsilon\cdot\ 1+3Bi+3Bi_r} \\ +\exp\left(-\frac{\upsilon\cdot\ 3+\xi}{P_2}\right)\cdot a\ 3\ =0 \tag{32}$$

The solution $a(\psi)$ were obtained:

$$a\ \psi\ =\frac{Exp\left(-3\frac{\upsilon}{P_2}+\frac{3\cdot\sqrt{P_2^2\cdot\ P_2-\upsilon\ \cdot\upsilon}}{P_2^2}+\frac{\upsilon\cdot\ 3+\xi}{P_2}-\frac{2\cdot\sigma_r^2}{\sigma_0^2}\right)}{\left(1+Exp\left(\frac{6\cdot\sqrt{P_2^2\cdot\ P_2-\upsilon\ \cdot\upsilon}}{P_2^2}\right)\right)\cdot\upsilon\cdot\ 1+3Bi+3Bi_r}\cdot \\ \left(Exp\left(\frac{P_2\cdot\upsilon-\sqrt{P_2^2\cdot\ P_2-\upsilon\ \cdot\upsilon}\ \cdot\psi}{P_2^2}\right)\right. \\ \left.+Exp\left(\frac{\left(P_2\cdot\upsilon+\sqrt{P_2^2\cdot\ \left(P_2-\upsilon\ \right)\upsilon}\ \cdot\right)\psi}{P_2^2}\right)\cdot\ \left(-3+\zeta\ \right)\right) \tag{33}$$

and therefore the complete solution:

$$\theta_{sa}\ \xi,\psi\zeta\ =\theta_1\ \zeta\ +\theta_2^+\ \xi,\psi\ = \\ -\frac{Exp^{-2\frac{\sigma_r^2}{\sigma_0^2}}\ -3+\zeta}{\upsilon\cdot\ 1+3Bi+3Bi_r}+a\ \psi\ \cdot Exp\left(-\upsilon\frac{\xi+\psi}{P_2}\right) \tag{34}$$

4.4 Semi-Analytical Solution Results

The solution was obtained using, for the two types of tests (def_0-def-$_6$), different parameter values as shown in the Table. 11. The coefficients P_1 and P_2 have been introduced in order to obtain a valid solution for all defocus values and therefore for each radius beam value (r). Remembering to have defined $x_{ref}=\frac{\alpha}{v}$, therefore independent of r_{ref}, we noticed how, by choosing the radius of the spot as reference, the solution was strongly dependent on this value, allowing to obtain a solution valid only for a fixed value of r.

Table 11. Proportionality Coefficients.

def	P1	P2
0	0.142857	11.5
-6	0.337838	10.9

We have therefore done so to link r_{ref} to x_{ref} and to the defocus value through the coefficients P1 and P2. After obtaining the temperature profile corresponding to the z = 0 plane (Figure 12) using a semi-analytical solution, the isothermal surface corresponding to 770 ° K was obtained (Figure 13).

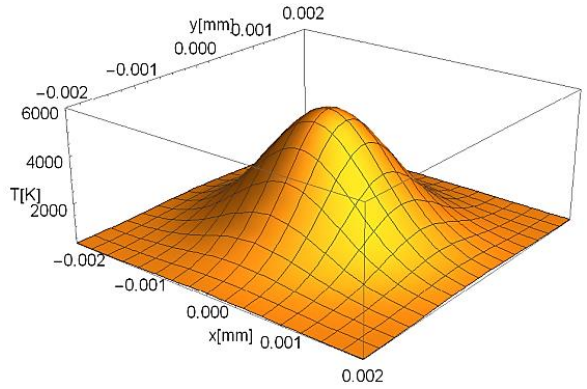

Figure 12. SA 5AL Temperature profile corresponding to the z = 0 plane.

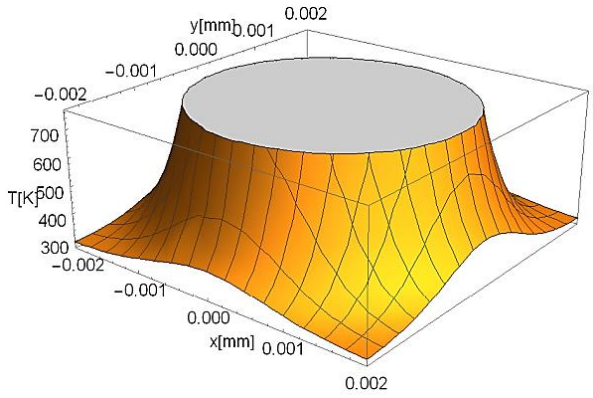

Figure 13. SA 5AL Temperature profile corresponding to the z = 0 plane; isothermal surface corresponding to 770 K.

Also, in this case the data have been fitted using an ellipse (Table 12).

Table 12. Fit Parameter –SA.

	1AL.	2AL	3AL	5AL	8AL	9AL
a	1.302	1.337	1.336	1.642	1.669	1.691
b	1.264	1.298	1.318	1.538	1.602	1.622
X_0	9.550	9.700	8.190	9.400	8.500	8.500
Y_0	10.00	10.00	10.00	10.00	10.00	10.00
ρ_x	2.603	2.674	2.673	3.285	3.339	3.382
ρ_y	2.528	2.596	2.636	3.077	3.204	3.245
w_z	2.40	2.58	2.88	2.87	3.18	3.40
Fit Err %	0.38	0.47	0.39	0.38	0.39	0.42
Tmax [K]	13932	16670	16690	5589	6095	6434

and subsequently the profiles of the isotherms were compared (Figures 14-16).
From the comparison it is evident that the error on ρ_y is very small (Table 13). As well as for the maximum temperature. Significantly greater is the error on ρ_x, but not relevant in this study and for our purposes.

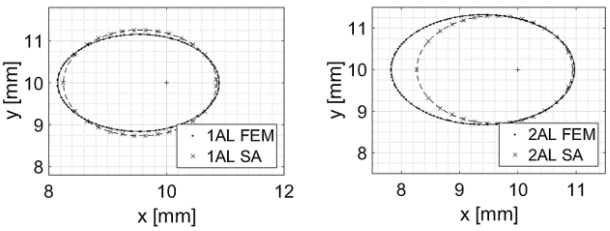

Figure 14. Isotherms corresponding to the melting point FEM vs SA; 1AL, 2AL.

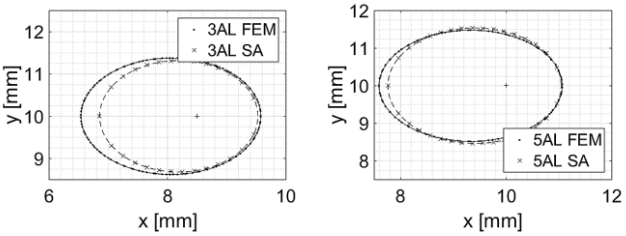

Figure 15. Isotherms corresponding to the melting point FEM vs SA; 3AL, 5AL.

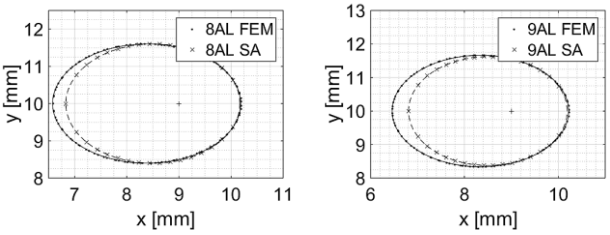

Figure 16. Isotherms corresponding to the melting point FEM vs SA; 8AL, 9AL.

Table 13. Comparison of Numerical and Semi-Analytical Solutions.

	FEM		SA		Err %	
	Tmax [K]	ρy [mm]	Tmax [K]	ρy [mm]	Tmax [K]	ρy [mm]
1AL	14294	2.318	13932	2.528	2.5	8.5
2AL	16945	2.649	16670	2.596	1.6	3.2
3AL	17096	2.756	16690	2.636	2.4	4.4
5AL	5977.8	2.961	5589	3.076	6.7	3.8
8AL	6418.9	3.201	6095	3.204	5.1	0.1
9AL	6823.8	3.329	6433	3.245	5.8	2.5

An error greater than 5% is found only in relation to the 1AL test, while the average error is equal to 3.75 %. In order to obtain a solution that is also valid for different defocus values, the coefficients P1 and P2 have been linearly interpolated to the respective defocus values def_0 and def_{-6}, and the relations P_1 (def) and P_2 (def) have been obtained :

$$\begin{cases} P_1(def)=0.0314\cdot def+0.1493 \\ P_2(def)=-0.1\cdot def+11.5 \end{cases} \quad (35)$$

Two further tests were then carried out at the defocus values def_{-4}, def_{-8} using the respective coefficients as shown in Table.14.

Table 14. Test Coefficients and Parameters.

	P1	P2	P[W]	v[mm·s-1]	def[mm]	d[mm]
4AL	0.2749	11.1	3000	50	-4	0.71
6AL	0.4005	10.7	3500	50	-8	1.32

First, the semi-analytical solution was evaluated, extrapolating the temperature profiles corresponding to the fusion isotherm (Table 15, Figures 17-18).

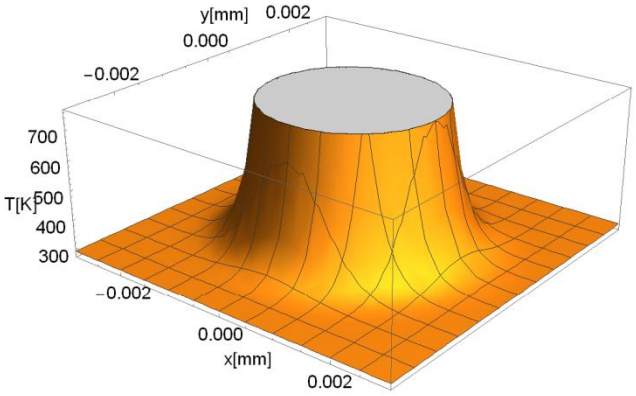

Figure 17. SA, test 4AL, Temperature profile corresponding to the z = 0 plane. ; isothermal surface corresponding to 770 K.

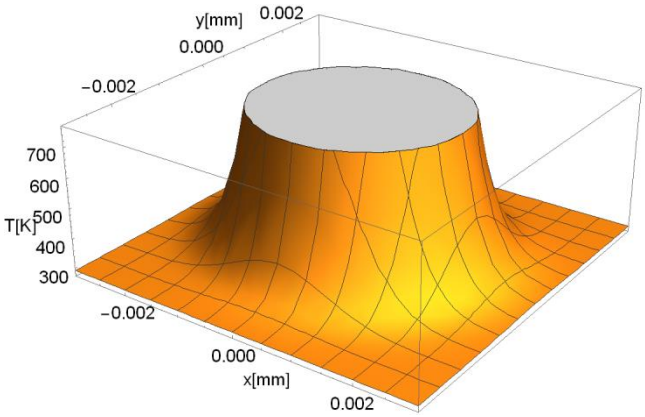

Figure 18. SA, test 6AL, Temperature profile corresponding to the z = 0 plane; isothermal surface corresponding to 770. K.

Table 15. Fit Parameter –de focus -4,-8. FEM Tests.

	4AL.		6AL	
	FEM	SA	FEM	SA
a	1.534	1.493	1.764	1.725
b	1.329	1.421	1.497	1.593
X_0	9.422	9.400	9.351	9.400
Y_0	9.999	10.000	10.000	10.000
ρ_x	3.067	2.986	3.529	3.067
ρ_y	2.659	2.821	2.993	3.126
Fit Err %	0.29	0.51	0.34	0.54
w_z [mm]	2.60	2.60	2.87	2.87
Err %	2.2	5.1	4.1	8.1
Tmax [K]	7393	7159	4547	4479
Dev.St [K]	55.7	/	29.5	/

Subsequently after having carried out the tests through FEM simulation and extrapolated the profiles corresponding to the fusion isotherm (Table 15),

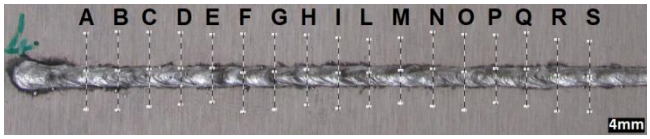

Figure 19. Test 4AL welding trace.

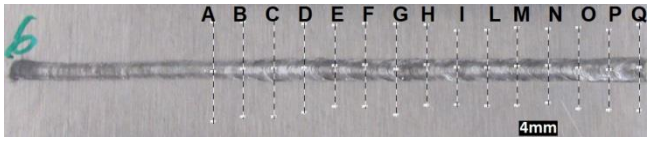

Figure 20. Test 6AL welding trace.

and it is compared to the width of the melt zone derived from experimental tests (Figures 19-20). Also in this case the error is less than 5%. Overall, the FEM tests were assessed with a maximum inaccuracy of 4.3% and an average err of 2.7%.

The isotherms corresponding to the melting point, obtained through FEM simulation and semi-analytical solution, are then compared (Table 16, Figures 21-22).

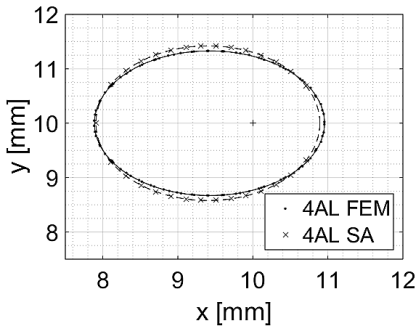

Figure 21. Isotherms corresponding to the melting point, FEM vs SA at time = 0.3 s Test 4AL..

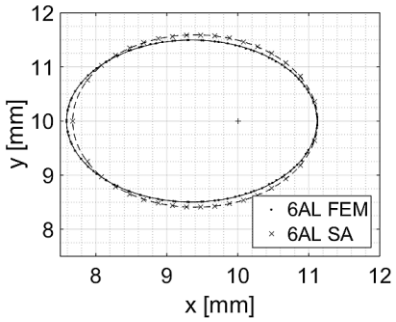

Figure 22. Isotherms corresponding to the melting point, FEM vs SA at time = 0.3 s Test Test 6AL.

Table 16. Tests at de focus -4,-8. FEM vs SA.

		ρy [mm]	ρy err %	Tmax [K]	Tmax err %
4AL	SA	2.821	6	7159	3.2
	FEM	2.993		4547	
6AL	FEM	2.659	4.3	7393	1.5
	SA	3.126		4479	

In this case the error is slightly higher (Table 16), but by appropriately modifying the proportionality coefficients it is possible to obtain a more accurate solution. Nonetheless, the total average error remains at an acceptable 4.1%.

5. Conclusions

We have seen how the semi-analytical solution recovers, with a small error, the value of the width of the melted zone. The semi-analytical solution has a strong dependence on the parameters involved, in particular on the value of the diameter of the laser beam. This means that having chosen the trial function for a given defocus value, the solution is valid only for the combined values of P and v at that fixed def value. In order to make the solution valid also for other defocus values, the proportionality coefficients have been

introduced. In particular, the coefficient P_1 refers to the reference quantity $r_{ref} = P_1 \cdot x_{ref}$, and serves to correct the value of ρ_y, while the coefficient P_2, referred to the trial function, has an effect on the maximum temperature.

So, after defining the proportionality coefficients to the defocus def_0 and def_{-6} values, the coefficients P1 and P2 have been linearly interpolated to the respective defocus values, and the relations P1 (def) and P2 (def) have been obtained. In this way it was possible to use a single trial function capable of providing a well approximated solution (err 5%), in terms of maximum temperature and ρ_y, as the working parameters (P, v, d) vary. This allowed it to value the emissivity [35] after setting parameters and measuring the width of the melted zone ($w_{mz} = \rho_y$) by SA solution.

Nomenclature

d	Beam diameter	mm
r_0	Beam radius	mm
def	Focal beam waist	mm
v	Welding speed	mm s^{-1}
w_z	Width of the melted zone	mm
ρ_y	Isotherm corresponding to the melting point	mm
P	Laser power	W
L_x	Slab length	mm
L_y	Slab width	mm
L_z	Slab depth	mm
C_{abs}	Absorption coefficient	/
k	Thermal conductivity	W $m^{-1}K^{-1}$
h	Thermal convection coefficient	W $m^{-2}K^{-1}$
ε	Emissivity	/
ρ	Mass density	Kg m^{-3}
α	Thermal diffusivity coefficient	m^2 s^{-1}
c_p	Specific heat.	J kg^{-1} K^{-1}
a	Radius of the X axis of the non-tilt ellipse	mm
b	Radius of the Y axis of the non-tilt ellipse	mm
φ	Orientation of the ellipse (tilt)	rad
X_0	Center at the X axis of the non-tilt ellipse	mm
Y_0	Center at the Y axis of the non-tilt ellipse	mm
ρ_x	Size of the long axis of the ellipse	
P_1	Proportionality coefficients	/
P_2	Proportionality coefficients	/
θ	Dimensionless temperature	/
ΔT_{ref}	Reference temperature	K
x_{ref}	Reference length	mm
r_{ref}	Reference radius	mm
t_{ref}	Reference time	s
v_{ref}	Reference velocity	m s^{-1}
ξ	Dimensionless space variable	/
ψ	Dimensionless space variable	/
ζ	Dimensionless space variable	/
FEM	Finite element method	/
B_i	Biot number	
$\dot{q}_g$	Gaussian source	W m^{-3}

References:

[1] P. Kumar, A. N. Sinha, "Studies of temperature distribution for laser welding of dissimilar thin sheets through finite element method", *J Braz. Soc. Mech. Sci., Eng.* 40, 455, 2018.

[2] M Miccio, R. Pierri, G. Cuccurullo, A. Metallo, P. Brachi, "Process intensification of tomato residues drying by microwave heating: experiments and simulation", *Chem. Eng. Process. Process Intensif.*, 156, 2020.

[3] I. Smurov, M. Doubenskaia, *Laser-Assisted Fabrication of Materials*, Springer Series in Materials Science 161, 373-422, 2013.

[4] T. Staudt, E. Eschner, M. Schmidt, "Temperature determination in laser welding based upon a hyperspectral imaging technique", *Manufacturing Technology*, CIRP Annals, 68 (1), 225-228, 2019.

[5] M. Doubenskaia , M. Pavlov , S. Grigoriev , I. Smurov, "Definition of brightness temperature and restoration of true temperature in laser cladding using infrared camera", *Surface and Coatings Technology* 220, 244-247, 2013.

[6] D. Rosenthal, *The Theory of Moving Sources of Heat and its Application to Metal Treatments*, Metals Handbook, 1981, 9th Ed., TranSASME, 68, pp. 3515-3528. 17 ASM, Metal Park, OH 1946.

[7] V. Alfieri, F. Caiazzo, V. Sergi, "Autogenous laser welding of AA2024 aluminum alloy: Process Issues and Bead Features", *Procedia CIRP*, 33, 2015.

[8] A. M. Leitner, T. Leitner, A. Schmon, K. Aziz, G. Pottlacher, "Thermophysical Properties of Liquid Aluminum", *Metall Mater Trans* A 48, 3036–3045, 2017.

[9] Q. G. Meng, H. Y. Fang, J. G. Yang, S. D. Ji, "Analysis of temperature and stress field in Al alloy's twin wire welding", *Theoretical and Applied Fracture Mechanics*, 44 (2), 178−186, 2005.

[10] E. Kaschnitz, W. Funk, T. Pabel, "Electrical resistivity measured by millisecond pulse-heating in comparison to thermal conductivity of the aluminum alloy Al-7Si-0.3Mg at elevated temperature", *High Temperatures-High Pressures*, , 43 (2), 175-191, 2014.

[11] K. Narender, A. S. M. Rao, K. G. K. Rao, N. G. Krishna, "Temperature Dependence of Density and Thermal Expansion of Wrought Aluminum Alloys 7041, 7075 and 7095 by Gamma Ray Attenuation Method", *Journal of Modern Physics*, 4 (3), 2013.

[12] M. Bjelić, K. Kovanda, L. Kolařík, M. N Vukićević, "Numerical modeling of two-dimensional heat-transfer and temperature-based calibration using simulated annealing optimization method: Application to gas metal arc welding", *Thermal Science*, 20, 255-265, 2016.

[13] C. Ratti, A. S. Mujumdar, *Infrared Drying*, Handbook of Industrial Drying by Taylor & Francis Group, LLC, 2006.

[14] J. Heigel, P. Michaleris, E. Reutzel, "Thermo-mechanical model development and validation of directed energy deposition additive manufacturing of Ti-6Al-4V", *Addit. Manuf.*, 5, 9–19, 2015.

[15] Z. Fan, L. Frank, "Numerical modeling of the additive manufacturing (AM) process of titanium alloy", *Titanium Alloys—Towards Achieving Enhanced Properties for Diversified Applications, A.K.M. Ed.*, 3–28. 2012.

[16] R. Paschotta, *Encyclopedia of Laser Physics and Technology*, Wiley-VCH: Berlin, Germany, 2008.

[17] K. Suresh Kumar, T. Sparks, F. Liou, "Parameter determination and experimental validation of a wire feed Additive Manufacturing model*", International Solid Freeform Fabrication Symposium*, Austin, TX, USA, 2015.

[18] C. Wen, I. Mudawar, "Experimental investigation of emissivity of aluminum alloys and temperature determination using multispectral radiation thermometry (MRT) algorithms", *J. Mater, Eng. Perform*, 11, 551–562, 2002.

[19] W. Steen, J. Mazumder, *Laser Material Processing*, Springer: Berlin, Germany, 2010.

[20] AWS, *Specification for Fusion Welding for Aerospace Applications*, American Welding Society, Miami, Fla, USA, 2001.

[21] W. W. Duley, *Laser welding*, John Wiley and Sons Inc., New York, 1999.

[22] M. Doubenskaia, I. Zhirnov, V. I. Teleshevskiy, Ph. Bertrand, I. Smurov, "Determination of True Temperature in Selective Laser Melting of Metal Powder Using Infrared Camera", *Materials Science Forum*, 834, 93-102, 2015.

[23] A. Mosavia, F. Salehib, L. Nadaie, Z. Karolyc, N. Gorjid, "Modeling the temperature distribution during laser hardening process", *Results in Physics*, 16, 2020.

[24] J. Sundqvista, A.F.H. Kaplana, L. Shachafb, C. Kongc, "Analytical heat conduction modelling for shaped laser beams", *Journal of Materials Processing Tech.*, 247,48–54, 2017.

[25] D. Rosenthal, "Mathematical theory of heat distribution during welding and cutting", *Weld. J.*, 20 (5), 220–234, 1941.

[26] N. Rykalin, A. Uglov, A. Kokora, O. Glebov, *Laser Machining and Welding*, Mir Publishers, Moscow, 1978.

[27] H. Carslaw, J. Jaeger, *Conduction of Heat in Solids*, Oxford Science Publications, 1990.

[28] T.W. Eagar, N.S. Tsai, "Temperature fields produced by traveling distributed heat sources", *Weld. J.* 62 (12), 346–355, 1983.

[29] J. Goldak, A. Chakravarti, M. Bibby, *A double ellipsoid finite element model for welding heat sources*, IIW Doc. No. 212-603-85, "A new finite element model for welding heat sources", *Metall Mater Trans B 15*, 299–305, 1984.

[30] N.T. Nguyen, A. Otha, K. Matsuoka, N. Suzuki, Y. Maeda, "Analytic solutions for transient temperature of semi-infinite body subjected to 3-D moving heat sources*", Weld. Res. Suppl.*, 265–274, 1999.

[31] N.T. Nguyen, Y.-W. Mai, S. Simpson, A. Otha, "Analytical approximate solution for double ellipsoidal heat source in finite thick plate", *Weld. Res.*, 82–93, 2004.

[32] M. Van Elsen, M. Baelmans, P. Mercelis, J.P. Kruth, "Solutions for modelling moving heat sources in a semi-infinite medium and applications to laser material processing*", International Journal of Heat and Mass Transfer*, 50 (23), 4872–4882, 2007.

[33] T. F. Flint, J. A. Francis, J. R. Yates, "Analytical solutions of the transient thermal field induced in finite bodies with insulating and convective boundary conditions subjected to a welding heat source", *Transactions*, SMiRT-22, San Francisco, California, USA, 2013.

[34] R. Forslunda, A. Snisa, S. Larsson, "Analytical solution for heat conduction due to a moving Gaussian heat flux with piecewise constant parameters", *Appl. Math. Model.*, 66, 227-240, 2019.

[35] A. Metallo , "Emissivity Prediction for an IR Camera During Laser Welding of Aluminum", *International Journal of Thermodynamics*, 25(4), 24-34, 2022.